PROCEEDINGS OF SPIE

Characterization of opto-acoustic color mapping for oxygen saturation of blood using biologically relevant phantoms

Jason Zalev, Lisa M. Richards, Bryan A. Clingman, Jeff Harris, Gisela L. G. Menezes, et al.

SPIE.

Characterization of Opto-acoustic Color Mapping for Oxygen Saturation of Blood using Biologically Relevant Phantoms

Jason Zalev[a,b], Lisa M. Richards[a], Bryan A. Clingman[a], Jeff Harris[a], Gisela L. G. Menezes[a],
Carlos Avila[a], Allison Bertrand[a], Xavier Saenz[a], Edgar Cantu[a], Steve Miller[a],
Alexander A. Oraevsky[c], Michael C. Kolios[b]

[a]Seno Medical, Inc., San Antonio, Texas, USA
[b]Department of Physics, Ryerson University, Toronto, Ontario, Canada
[c]Tomowave Laboratories, Houston, Texas, USA

ABSTRACT

Opto-acoustic imaging involves using light to produce sound waves for visualizing blood in biological tissue. By using two different optical wavelengths, diagnostic images of blood oxygen saturation can be generated using endogenous optical contrast, without injection of any external contrast agent and without using any ionizing radiation. The technology has been used in recent clinical studies for diagnosis of breast cancer to help distinguish benign from malignant lesions, potentially reducing the need for biopsy through improved diagnostic imaging accuracy. To enable this application, techniques that can accurately map and effectively display small differences in oxygen saturation are necessary.

We analyze the ability of an opto-acoustic imaging system to display a colorized parametric map for oxygen saturation of blood using biologically-relevant opto-acoustic phantoms. The relationship between colorized image output and known oxygen saturation values is examined. To mimic breast tissue, a material with closely matching properties for optical absorption, optical scattering, acoustic attenuation and speed of sound is used. The phantoms include two vessels filled with whole blood at oxygen saturation levels determined using a gold-standard sensor-based approach. A flow system with gas-mixer and membrane oxygenator adjusts the oxygen saturation of each vessel independently. Data is collected with an investigational Imagio® breast imaging system. An opto-acoustic relative color map is generated using a novel statistical mapping approach. In addition, we propose a technique to characterize the ability to distinguish small differences in oxygen saturation as the oxygenation level is varied. When applied to the phantom, with reference vessel at 99% saturation, hematocrit of 42% and depth of 1.5cm, a contrast distinction threshold was reached when an adjusted vessel achieved a difference of approximately 4.6% saturation compared to the reference.

Keywords: opto-acoustic colorization, blood oxygen saturation, tissue realistic phantom, relative color map

1. INTRODUCTION

Over the past decade, a growing community of researchers, clinicians and device manufacturers have been investigating and developing translational opto-acoustic (OA) imaging technologies with the aim of improving clinical care for several diseases.[1–5] One promising technique is OA imaging combined with ultrasound (OA/US).[6–13] Structural and functional information about vascularity and blood oxygen saturation (s_{O_2}) can be visualized with OA, while morphological and anatomical information can be obtained with ultrasound. The combination of these two modalities is advantageous for breast cancer diagnosis, since each modality provides information that is complementary to the other. In ultrasound, which is commonly used to assess and characterize breast masses, there is large overlap between benign and malignant image features, which results in false positive cases that must be confirmed with subsequent biopsy. However, OA can provide functional information about the metabolism of tumors by imaging blood and vascular structure, which may further differentiate benign from malignant masses.

Further author information: (Send correspondence to J.Z.)
J.Z.: E-mail: jzalev@senomedical.com
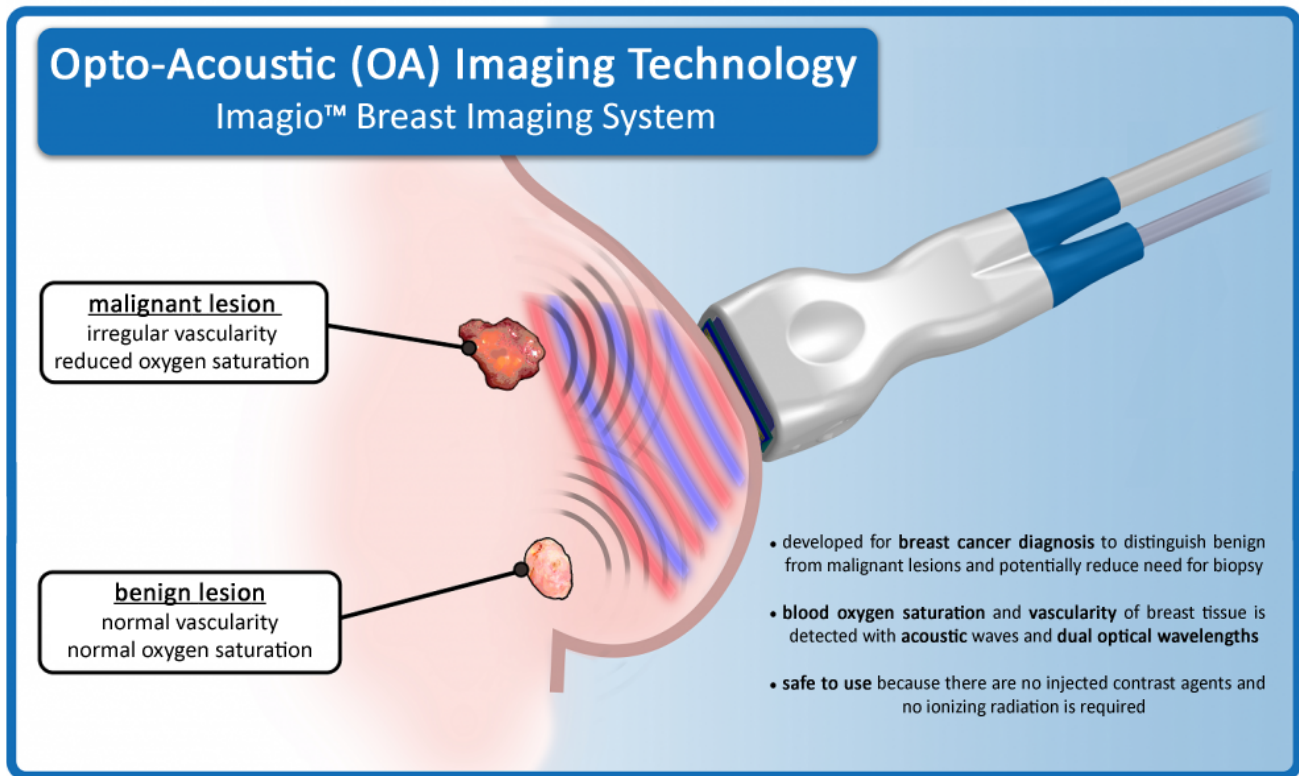M.C.K.: E-mail: mkolios@ryerson.ca

Figure 1: Opto-acoustic imaging technology for breast cancer diagnosis. A hand-held OA probe uses light and sound to visualize benign and malignant lesions.

Breast biopsy is the current standard of care for diagnosing or ruling out cancer in a mass that has been detected. It is estimated that over 1.6 million breast biopsies are performed in the United States each year.[14, 15] A large percentage of these biopsies are negative, which is due to low positive predictive value (PPV) of the imaging modalities presently used for assessment.[15, 16] Biopsies involve extracting a sample of tissue using a needle, or through surgical excision, and are the most invasive part of the breast cancer diagnostic process. A possible reduction in the total number of breast biopsies could greatly improve patient care and potentially reduce overall health care costs.[15] Therefore, an immediate goal of OA/US imaging is to potentially allow downgrading mildly suspicious masses to a category where biopsy is not required, without increasing the number of missed cancer cases.[6, 8, 10, 11]

In a recent Pivotal study[7] consisting of 2105 subjects from 16-sites, clinical OA/US images were collected using an investigational Imagio breast imaging device (see Figure 1). In the study, seven blinded and independent radiologists assessed 1079 benign and 678 malignant breast masses. Each mass was numerically scored in five different categories for the presence of specific opto-acoustic features. Several types of OA/US image maps were used to assess the lesions, including one map for conventional ultrasound. Colorized functional OA information was overlaid on the ultrasound map to indicate relative oxygen saturation and the presence of hemoglobin. In the study, OA/US was found to exceed diagnostic specificity of ultrasound by 14.9%. For negative OA/US findings, a maximum pre-test probability for malignancy of 17.8% could potentially be downgraded with OA/US to a post-test probability of 2% to avoid biopsy. The most significant features found to distinguish benign from malignant lesions were the presence of radiating vessels in the peripherial zone, and the presence of multiple boundary zone vessels. Benign and malignant lesions were both commonly found to contain strong relative internal deoxygenation, but the absence of internal deoxygenation was more likely for benign lesions.

OA/US maps for a malignant lesion are shown in Figure 2. The relative spatial distribution of s_{O_2} is considered an important parameter for assessing differences between benign and malignant lesions. For qualitative imaging,
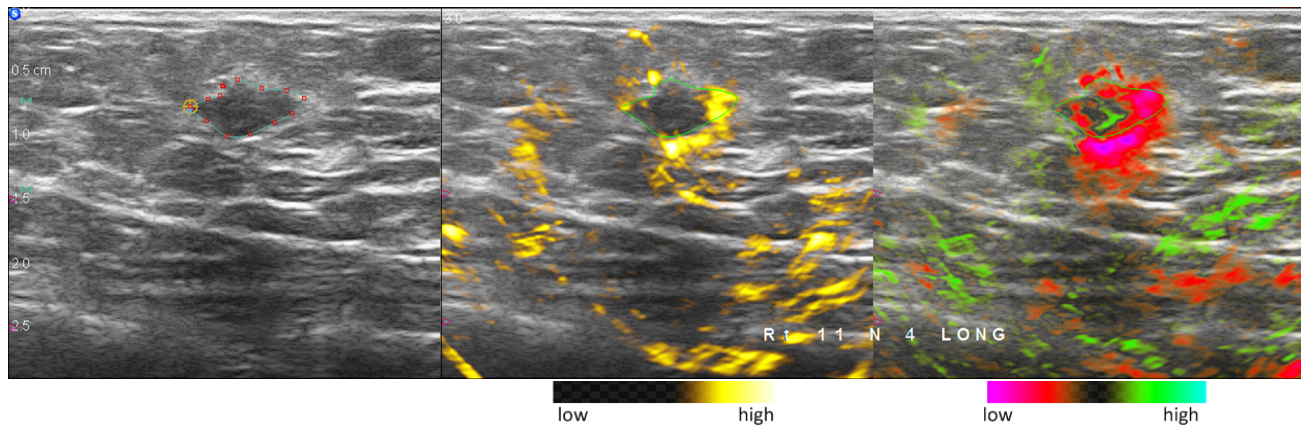
Figure 2: OA/US images of malignant lesion. The image maps are Ultrasound (left), OA Total (center), and OA Relative (right). The central nidus of the lesion is segmented with a cyan color outline. Histopathology conducted after excision revealed this grade III invasive ductal carcinoma (GR3-IDC) had extensive internal necrosis. This may account for the lack of internal OA signal within the central nidus, as vessels are not present in the necrotic region. In OA Total, strong signal (yellow) due to hemoglobin is observed in the boundary zone of the lesion. Strong relative de-oxygenation (red) is observed in the boundary zone of the OA Relative map. The image features are consistent with neoangiogenesis and are interpreted here as signs of malignancy.

accurate diagnosis involves proper interpretation of color mapped images and an understanding of how images relate to tumor physiology. Therefore, it is necessary to characterize the measurement capabilities of imaging devices using materials with properties that are similar to actual biological tissue.

To mimic light and sound propagation in tissue, several types of OA phantoms have been investigated previously in the literature.[17–22] The approach of Vogt et al. (2016) described producing biologically relevant OA phantoms in a PVCP (polyvinyl chloride plastisol) based material with tunable optical and acoustical properties.[19] Vogt et al. also described using PVCP phantoms with bovine blood oxygenated to controlled levels for OA performance evaluation.[23, 24]

In this paper, an approach for characterizing *qualitative* OA color maps of s_{O_2} is described, which relates RGB image colorization to known oxygen saturation values. To achieve this, we perform *quantitative* measurement using biologically relevant phantoms and bovine blood at controlled oxygenation levels. The purpose for the testing described here is *to determine the ability to distinguish small differences* in s_{O_2} for varied measurement conditions. The dual-vessel perfusion flow system that is described can also be used to assess several other performance parameters, but additional testing that was performed is beyond the scope of this paper.

2. OPTO-ACOUSTIC IMAGING

2.1 Physical principles of OA

OA involves several physical principles that make it ideally suited for diagnostic breast imaging, especially when the modality is fused with grayscale ultrasound. Using light means that OA visualizes the optical contrast of tissue. The contrast can be optimized for detecting certain molecules through optical wavelength selection, which makes OA capable of providing functional information related to tumor growth and metabolism. Furthermore, due to the composition of breast tissue, scattered light can penetrate to a depth of several centimeters, which is suitable for clinical applications. The probe measures acoustic waves, which are generated by blood and other tissue structures when they are illuminated. By precisely measuring the timing of when the acoustic waves are received, images are formed that display the functional composition of tissue. The probe is also capable of acquiring conventional ultrasound images, which are co-registered and displayed simultaneously with OA. Therefore, in OA/US imaging is it possible to present anatomical structure overlayed with functional information related to vascularity.

The ability to directly visualize blood and s_{O_2} can potentially give clinicians the ability to perform more accurate diagnosis.[6–10] Typical benign lesions have normal blood vessels and normal oxygen saturation. Malignant lesions are metabolically more active, and tend to have higher vascularity, irregular blood vessels and decreased oxygen saturation.[25] An example showing OA/US image maps from a malignant lesion is provided in Figure 2.

2.2 OA signal generation from blood and biological tissue

Blood is the strongest optical absorber in biological tissue for near-infrared light. It contains both oxygenated hemoglobin (HbO_2) and de-oxygenated hemoglobin (HbR), which are molecules that have different wavelength-specific optical absorption. For example, light at 757nm is absorbed more strongly by HbR compared to HbO_2, but at 1064nm this is reversed.

When molecules absorb light, they heat up, which causes thermal expansion. The *optical absorption coefficient* $\mu_a(\lambda, \mathbf{x})$ of a substance determines the amount of light that it can convert to heat. This is a function of optical wavelength λ. In a non-uniform material such as biological tissue, it is also a function of position $\mathbf{x} = (x, y, z)$, since molecular composition varies spatially. When a material is heated rapidly, pressure is generated. The amount of pressure p_0 is proportional to a material property called the *Grüneisen parameter* $\Gamma(\mathbf{x})$, which quantifies how added heat is converted to pressure. The *radiant fluence* $\Phi(\lambda, \mathbf{x})$ is the amount of light, at wavelength λ, that reaches position $\mathbf{x}$ during the entire time interval of the heating. Overall, the pressure generated, immediately following the rapid heating, is

$$p_0(\lambda, \mathbf{x}) = \mu_a(\lambda, \mathbf{x}) \times \Gamma(\mathbf{x}) \times \Phi(\lambda, \mathbf{x}). \tag{1}$$

The generated pressure $p_0(\lambda, \mathbf{x})$, called the *initial excess pressure*, corresponds to the amount of opto-acoustic signal that can be detected. Since blood has a much stronger μ_a compared to background tissue, the pressure generated from blood, and thus the OA signal it produces, is very strong. This results in high image contrast.

Optical absorption of blood depends on its s_{O_2} level. The s_{O_2} represents the percentage of hemoglobin that is oxygenated.[26–28] This can be determined from the *hemoglobin mass concentrations*, c_{HbO_2} and c_{HbR}, by

$$s_{O_2} = \frac{c_{HbO_2}}{c_{HbO_2} + c_{HbR}}. \tag{2}$$

The *total hemoglobin concentration* is

$$c_{tHb} = c_{HbO_2} + c_{HbR}. \tag{3}$$

A substance is often a mixture several different optically absorbing *chromophores*. The overall absorption coefficient of a substance is a weighted combination of each chromophore's absorption $\mu_{a,i}$ times its *volume fraction* $f_{v,i}$. Equivalently, the overall absorption coefficient can be written by adding the mass concentration c_i times the *optical extinction coefficient* ε_i for each chromophore.[29] Here, the subscript i represents an index number that denotes each chromophore. Thus,

$$\mu_a(\lambda) = \sum_i f_{v,i} \times \mu_{a,i}(\lambda) = \sum_i c_i \times \varepsilon_i(\lambda). \tag{4}$$

Biological tissue can be modeled as a mixture of HbR, HbO_2, melanin and also several other chromophores that have much weaker optical absorption (e.g., water and lipids). For example,

$$\mu_a(\lambda) = f_{v,HbO_2} \times \mu_{a,HbO_2}(\lambda) + f_{v,HbR} \times \mu_{a,HbR}(\lambda) + f_{v,melanin} \times \mu_{a,melanin}(\lambda)$$
$$+ f_{v,water} \times \mu_{a,water}(\lambda) + f_{v,lipids} \times \mu_{a,lipids}(\lambda) + \dots. \tag{5}$$

Melanin is present mainly in epidermal layer, but not in deeper tissue. For a homogeneous sample of sub-surface tissue or blood, the optical absorption coefficient $\mu_a(\lambda)$ is often computed by considering absorption only from hemoglobin. Thus,

$$\mu_a(\lambda) = c_{HbO_2} \times \varepsilon_{HbO_2}(\lambda) + c_{HbR} \times \varepsilon_{HbR}(\lambda). \tag{6}$$

This expression can also be grouped in terms of s_{O_2} and c_{tHb} as

$$\mu_a(\lambda) = c_{tHb} \times \big[s_{O_2} \times \varepsilon_{HbO_2}(\lambda) + (1 - s_{O_2}) \times \varepsilon_{HbR}(\lambda) \big]. \tag{7}$$

For whole blood, the hemoglobin concentration $c_{tHb,blood}$ is approximately 150 mg/mL.[29] The *hematocrit* level α_{hct} (the percentage of blood that is red blood cells) for whole blood is nominally 45%. In tissue, the apparent volume fraction of blood ranges from a negligible level to 100% for whole blood.[29]

The radiant fluence $\Phi(\lambda, \mathbf{x})$ in an illuminated medium is dependent on its wavelength-specific optical properties. This includes the optical absorption coefficient $\mu_a(\lambda)$, *optical scattering coefficient* $\mu_s(\lambda)$, and *anisotropy parameter* $g(\lambda)$.[29–31] In tissue, $\Phi(\lambda, \mathbf{x})$ can be approximated by assuming homogeneous optical properties and using a 1D model based on a wide-beam diffusion approximation.[30] In this case, at depth z and with surface exposure $q_0(\lambda)$, the fluence is

$$\Phi(\lambda, \mathbf{x}) = q_0(\lambda) \times e^{-\mu_{eff}(\lambda) z}, \tag{8}$$

where the *effective optical attenuation* coefficient $\mu_{eff}(\lambda)$ is

$$\mu_{eff}(\lambda) = \sqrt{3\mu_a(\lambda)\big(\mu_a(\lambda) + (1 - g)\mu_s(\lambda)\big)}. \tag{9}$$

For a tissue sample, the generated OA pressure can be obtained by combining equation (6) with equation (1). For wavelength λ at position $\mathbf{x}$, this is

$$p_0(\lambda, \mathbf{x}) = \Gamma(\mathbf{x}) \times \Phi(\lambda, \mathbf{x}) \times \big[c_{HbO_2}(\mathbf{x}) \times \varepsilon_{HbO_2}(\lambda) + c_{HbR}(\mathbf{x}) \times \varepsilon_{HbR}(\lambda) \big]. \tag{10}$$

Since multiple optical wavelengths are used, equation (10) is repeated for each wavelength. It is convenient to write this in matrix form. If two wavelengths are used, i.e. $\lambda_1 = 757$nm and $\lambda_2 = 1064$nm, this becomes

$$\underbrace{\begin{bmatrix} p_0(\lambda_1, \mathbf{x}) \\ p_0(\lambda_2, \mathbf{x}) \end{bmatrix}}_{\mathbf{p}(\mathbf{x})} = \Gamma(\mathbf{x}) \underbrace{\begin{bmatrix} \Phi(\lambda_1, \mathbf{x}) & 0 \\ 0 & \Phi(\lambda_2, \mathbf{x}) \end{bmatrix} \begin{bmatrix} \varepsilon_{HbO_2}(\lambda_1) & \varepsilon_{HbR}(\lambda_1) \\ \varepsilon_{HbO_2}(\lambda_2) & \varepsilon_{HbR}(\lambda_2) \end{bmatrix}}_{A(\mathbf{x})} \underbrace{\begin{bmatrix} c_{HbO_2}(\mathbf{x}) \\ c_{HbR}(\mathbf{x}) \end{bmatrix}}_{\mathbf{c}(\mathbf{x})}. \tag{11}$$

For each position $\mathbf{x}$, this can be written more compactly as

$$\mathbf{p} = A\mathbf{c}. \tag{12}$$

When measuring tissue, the vector $\mathbf{c}$ represents the unknown concentration values $c_{HbO_2}(\mathbf{x})$ and $c_{HbR}(\mathbf{x})$. These can be solved by inverting the 2×2 matrix in equation (12) at each position. This can be written

$$\mathbf{c} = A^{-1}\mathbf{p}. \tag{13}$$

For OA imaging, a map of the initial pressure $p_0(\lambda, \mathbf{x})$ is generally reconstructed by an imaging algorithm using data recorded from transducers, which corresponds to the vector $\mathbf{p}$.

To compute $s_{O_2}(\mathbf{x})$ and $c_{tHb}(\mathbf{x})$, the values of $c_{HbO_2}(\mathbf{x})$ and $c_{HbR}(\mathbf{x})$ from $\mathbf{c}$ in equation (13) can be substituted into equations (2) and (3).

Our approach for displaying qualitative parametric maps based on s_{O_2} and c_{tHb}, which uses a statistical mapping procedure, is presented in Section 3.2.

3. METHODS

3.1 Biologically relevant phantoms

To mimic breast tissue, a PVCP based opto-acoustic phantom was constructed as shown in Figure 3. The optical and acoustical properties were tuned[19] to have biologically relevant properties at 757nm and 1064nm optical wavelengths, using additives of TiO_2 and carbon black. The optical absorption coefficient μ_a, anisotropy parameter g, and the reduced scattering coefficient* μ'_s of the phantom were measured using inverse adding and doubling[32] as shown in Table 1.

Two vessels of inner diameter 1.6mm were embedded in the phantom. The vessels consisted of Teflon tubing and were sloped at a 17° incline to permit varying of depth during imaging. The vessels were connected to a perfusion flow system as shown in Figure 4 to independently control their s_{O_2} levels.

The vessels were filled with bovine blood (Innovative Research Inc., Catalog No.: IR1-040N). Bovine blood has optical properties that are similar to human blood.[33, 34] The bovine whole blood was treated with an anticoagulant (sodium citrate). The hematocrit concentration of the whole blood was analyzed by filling capillary tubes (Fisher, P/N: 22-362-574) with the blood sample and sealing one end with sealing compound (Fisher, P/N: 02-678). Samples were then placed in a micro hematocrit centrifuge for 5 minutes. Using calipers, the length

---

*The reduced scattering coefficient is related to the scattering coefficient by $\mu'_s = \mu_s(1 - g)$.

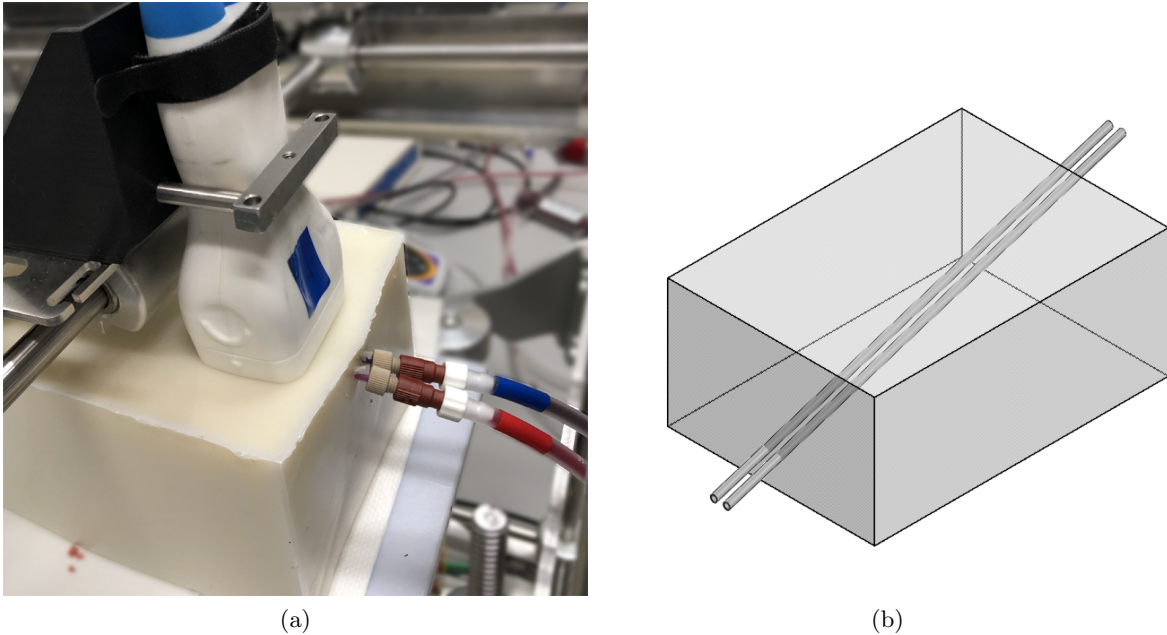| (a) | (b) |

Figure 3: PVCP based opto-acoustic phantom. Two vessels are filled with bovine blood at independently controlled s_{O_2} levels.

Table 1: Measured optical and acoustical properties of PVCP based phantom

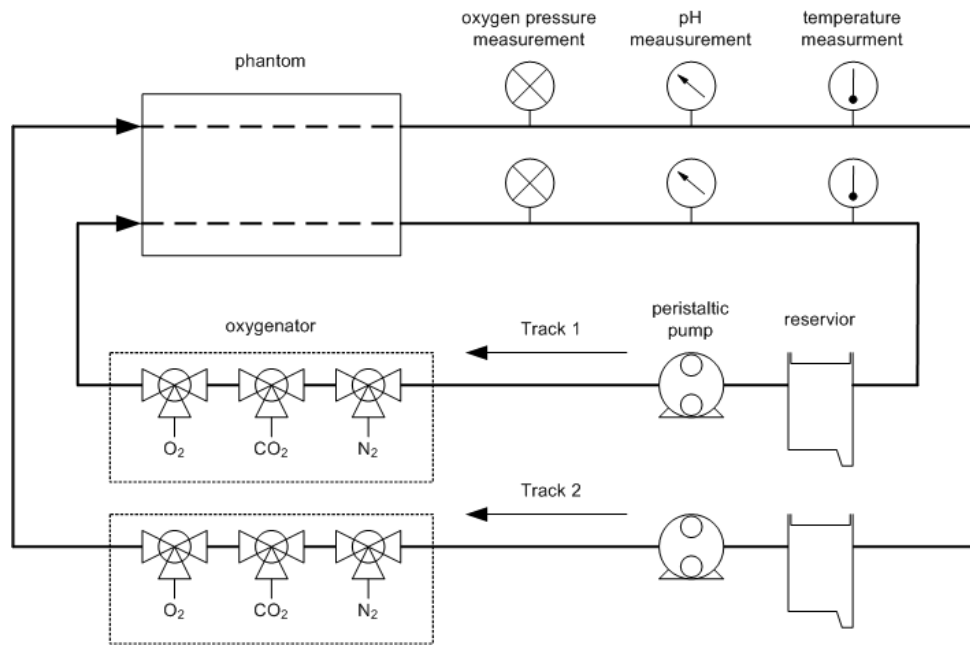| **Material**: PVCP (plastisol)		
Optical Properties	757nm	1064nm
Absorption μ_a (1/cm)	0.089 ± 0.014	0.279 ± 0.055
Reduced Scattering μ'_s (1/cm)	7.90 ± 0.20	6.14 ± 0.07
Anisotropy g (-)	0.80 ± 0.08	0.77 ± 0.01
Acoustical Properties		
Speed of sound (m/s)	1475	
Attenuation (dB/cm)	$0.9 - 8.3$	

Figure 4: Controlled s_{O_2} measurement apparatus. Two independent tracks of bovine blood at controlled oxygenation levels are circulated through the phantom with perfusion flow system. A gas-mixer delivers O_2, CO_2 and N_2 to a membrane oxygenator. Sensor readings for temperature, dissolved oxygen pressure and pH are used to monitor the s_{O_2} level.

of the hematocrit or red cell volume and the length of total volume were measured. The ratio represents the packed cell volume (PCV) which corresponds to the hematocrit level.

The perfusion flow system used a peristaltic pump (Masterflex, Model: 75728-10) that pulled blood from a reservoir to an membrane oxygenator (Permselect, Model: PDMSXA-2500), to balance the gas levels of oxygen, nitrogen, and carbon dioxide in the blood. The gas supply consisted of a tank of each pure compressed gas for each track. Each tank was connected to a gas-mixer (MCO, Model: GB 100), that controlled the flow and combined it into a single output connected to the oxygenator. To determine s_{O_2} level, the partial O_2 pressure, pH level, and temperature were monitored using sensors. A change in the CO_2 level had an influence on the pH level, and CO_2 was initially adjusted to establish a pH level of 7.4 using a pH meter (Denver Instruments, Model: UB-10). The partial O_2 pressure was measured by a pair of dissolved oxygen (DO) meters (Oakton, Model: DO-450), which also record temperature to $\pm 0.1°$C. The meters output DO as a percentage of the calibrated partial pressure of oxygen at atmospheric pressure. As shown in Figure 4, in each track, the blood flowed from the oxygenator directly to the phantom and then to the DO meters before returning to the reservoir.

A *gold standard* approach was used to determine known s_{O_2} levels for blood in both vessels, based on sensor readings. Oxygen saturation in blood varies according to known *hemoglobin dissociation curves*.[35] These curves model how s_{O_2} changes as a function of partial oxygen pressure, pH level and temperature, and to a lesser extent on partial pressure of CO_2 and the DPG (2,3-diphosphoglycerate) concentration. A mathematical relationship to determine oxygen saturation from these variables is described by Dash et al.[35] A Matlab function for computing s_{O_2} based on the Dash model was available for download and used in the present analysis.

An investigation of the measurement accuracy of using hemoglobin dissociation curves was also performed by varying input parameters in the Dash model and to compute error-bars for s_{O_2} measurement. It was determined that the highest accuracy occurs near full deoxygenation and full oxygenation, which is due to the lower slope portion of the oxygen dissociation curves, and greater uncertainty was found for mid-level s_{O_2} values.

3.2 Statistical Color Mapping

The optical properties and light propagation of breast tissue can vary significantly between subjects, depending on tissue composition and epidermal melanin concentration.[29] This represents a challenge for quantitative imaging, if conventional techniques are used to display information based on equation (13). However, for qualitative imaging the goal is to maximize the contrast of lesions compared to background tissue, rather than to measure precise numerical values of a parameter. With this in mind, we propose a practical and effective technique to automatically generate colorized parametric maps based on s_{O_2} and c_{tHb}. A statistical approach is used to qualitatively map estimated parameter values onto RGB image colorization. This enables displaying the relative spatial distribution of total hemoglobin and oxygen saturation in tissue.

The *statistical color mapping* technique[36] first analyzes statistics of a reference region of each image to automatically determine color scaling and offset parameters. Second, color mapping is performed to display opto-acoustic information using relative colorization. This visualizes structural and functional information from areas of strong blood oxygenation and total hemoglobin relative to background tissue.

The reference region is selected to include average background tissue. Commonly, it is set to encompass the entire mid-field tissue region. For analysis purposes, the reference region can also be set to the upper and lower bounds of a target of interest. Color mapping parameters are obtained by computing a mathematical characteristic applied to parameter values of the reference region. In particular, the average signal level of reference region is used as a color midpoint. A color scaling parameter is computed based on the standard deviation of the reference region to maximize the contrast level displayed. This qualitatively highlights regions
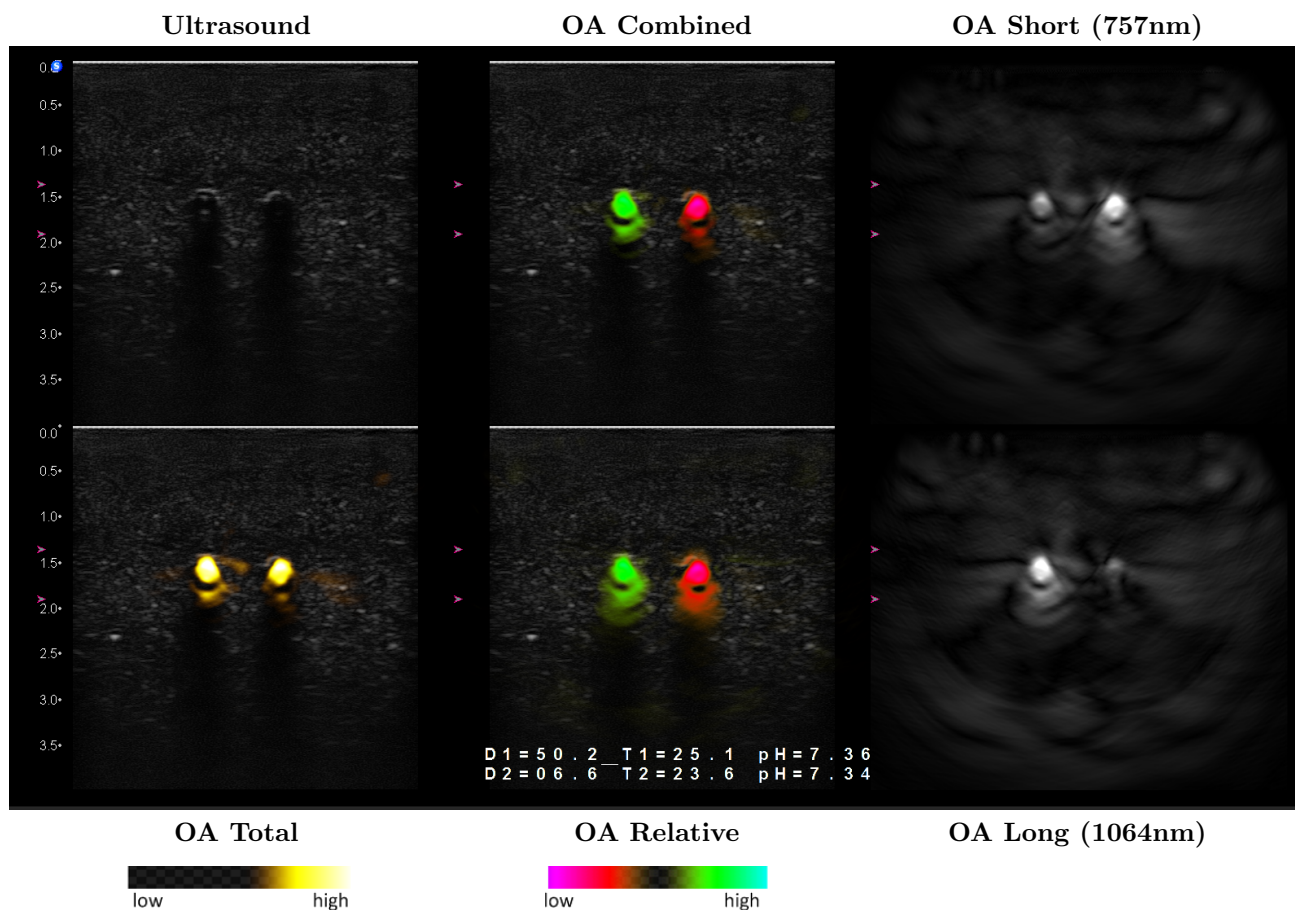

Figure 5: Oxygenated and de-oxygenated vessels in PVCP phantom displayed with six Imagio image maps. The measured s_{O_2} levels are 99% for Vessel 1 (left, green) and 31% for Vessel 2 (right, red).

of significance that have higher or lower levels of oxygen saturation than the reference level. In addition, a transparency mask is generated to permit only regions exceeding a specific colorization level to be displayed.

Three different color maps are computed by using this technique, which are then overlayed on ultrasound. The OA Total, OA Combined and OA Relative maps are shown in Figure 5. The computation for the OA Total map is the qualitative color mapping of the total hemoglobin estimate. Areas with high value appear yellow. Areas with low value are transparent. The computation for the OA Relative map is the qualitative color mapping of the blood-oxygenation saturation estimate. The transparency mask is based on the value for each pixel value being outside of an upper and lower range. Areas with high value appear green, while areas with low value appear red. Areas with mid-range values are transparent. The OA Combined map uses the same RGB values that were computed for OA Relative. The transparency mask of OA Combined is different from OA Relative. It is computed by combining the transparency of OA Total with the transparency of OA Relative to display signal that is strong in both maps.

4. RESULTS

The biologically-relevant PVCP based phantom was imaged using an investigational Imagio system. The positioning of the probe geometry relative to the phantom is shown in Figure 3. Images were collected while the s_{O_2} levels of both vessels were individually controlled using the perfusion flow system with gas-mixer, as described in Section 3.1. Sensor readings were continually monitored and recorded during image collection.

Figure 5 shows a captured Imagio image of the phantom, which consists of the six simultaneously displayed image maps. For purposes of this analysis, an individual six-on-one image corresponds to a single measurement in the collected dataset analyzed below. In each measurement, the circular cross-sections from both vessels are visible in each of the six maps. The depth of the vessels is 1.5cm, and the maximum imaging depth is set to 4cm. Conventional grayscale ultrasound is displayed in the top left section. OA Total (bottom left section) represents the total amount of OA signal and corresponds to the presence of hemoglobin. Both vessels appear yellow in this map. The OA Relative (bottom center) and OA Combined (top center) image maps qualitatively display s_{O_2} using relative colorization overlayed on ultrasound. Vessel 1 is at 99% s_{O_2} and appears green. Vessel 2 is at 31% s_{O_2} and appears red. In the OA Combined map, colorization is displayed for regions of strong signal in both OA Relative and OA Total maps. Since the vessels have strong hemoglobin and strong relative oxygenation, OA Relative and OA Combined look fairly similar.

The OA Short (top right section) and OA Long (bottom right section) image maps are generated from individual optical wavelengths of 757nm and 1064nm. In the OA Short and OA Long image maps, a different intensity for each vessel is observed because the optical absorption coefficient of blood is wavelength specific and depends on oxygen saturation. Observe that Vessel 2, which has a low s_{O_2} (31%), has a low signal in the long wavelength. However, Vessel 2 has strong signal for the short wavelength. Vessel 1, which has high oxygen saturation (99%) has moderately weak signal at the short wavelength, and strong signal in the long wavelength.

In Figure 6, the RGB image colorization of the phantom is displayed when s_{O_2} of both vessels is varied using the gas-mixer described in Section 3.1. The s_{O_2} of Vessel 1 is varied from full oxygenation to around 30%. Vessel 2 is varied from around 30% to full oxygenation. The hematocrit level was measured at 46%. The measured oxygen saturation of the vessels was determined from sensor readings and plotted as a function of sequential measurement number. Error-bars for the oxygen saturation measurements are shown. Analysis indicated that the measured oxygen saturation has higher uncertainty when s_{O_2} is further from the endpoints of 0% or 100% due to behavior of oxygen dissociation curves, as described in Section 3.1.

In each measurement of Figure 6, a six-on-one image (configured as shown in Figure 5) was collected, and the sub-region surrounding the two vessels in OA Combined was analyzed. A collage for the sub-region is presented, according to measurement number, that graphically shows the displayed image colorization of the vessels as the vessel s_{O_2} level was varied.

To quantitatively measure image colorization of each vessel, the RGB values in a window surrounding each vessel were mapped into numerical values in the range -1 to +1. The maximum deoxygenation from the color palate (red) corresponds to -1, and maximum oxygenation (green) corresponds to +1. By determining a color hue from RGB values, this permitted a one-to-one continuous mapping from the color palate that was not affected

by the overlay with grayscale ultrasound. To quantify the displayed colorization of the entire vessel, the average mapped value within its surrounding window was computed, but only for pixels with mapped values having a magnitude exceeding the median magnitude of the window, which avoided noise by skipping highly transparent pixels. This numerical result was plotted as the *measured image colorization* for each vessel.

For the proposed technique, we computed a single numerical value ΔM that characterizes the ability to distinguish small differences in oxygen saturation. This is shown in Figure 7. To do this, we performed measurements with Vessel 1 held at a constant fully oxygenated s_{O_2} level of 99%. Meanwhile, the s_{O_2} of Vessel 2 is varied from low oxygenation to full oxygenation. This reduces uncertainty in Vessel 1 s_{O_2} and facilitates measuring the point at which the loss of Vessel 2 contrast distinction is reached. For this test, the hematocrit level was measured at 42%. The sub-region surrounding the two vessels in OA Combined mode is displayed for each measurement as the s_{O_2} of Vessel 2 is varied. From the collage of sub-region images, it is observed that there is less distinction between the two vessels as their oxygen saturation measurements become closer together.
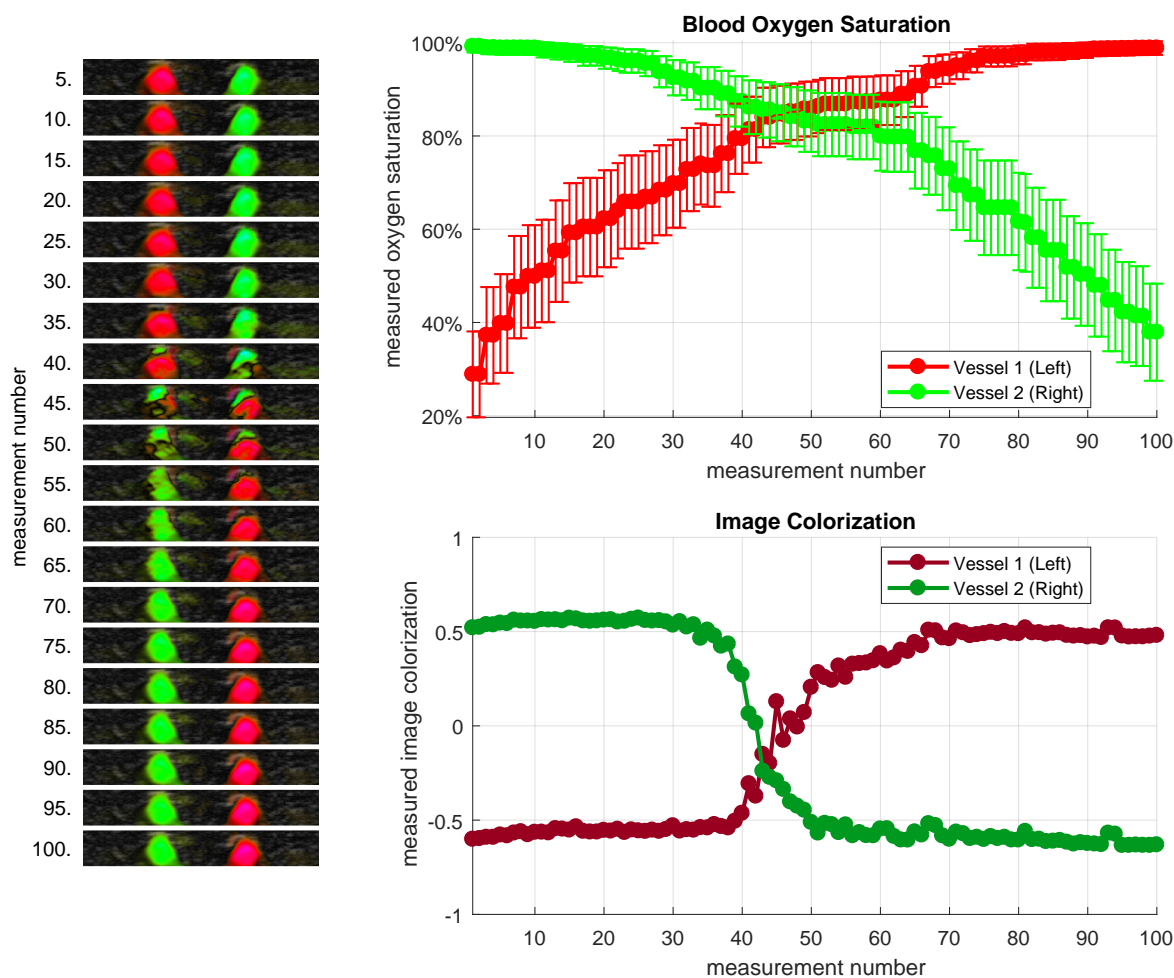

Figure 6: Characterization of RGB image colorization as oxygen saturation of Vessel 1 and Vessel 2 is varied in biologically relevant phantom of Figure 3. The *measured oxygen saturation* is determined from sensor readings (upper plot). Measurements are sequentially numbered. A subregion surrounding the two vessels from the OA Combined image map, which was acquired for each measurement, graphically indicates the displayed colorization (left). The *measured image colorization* is quantitatively determined from the OA Combined RGB image data of each measurement, which is mapped to a numerical value from -1 to +1 (lower plot).

We were interested in determining when the measured image colorization curves approach each other to within a pre-determined *contrast distinction threshold* ΔC. An empirically selected value of $\Delta C = 0.5$ is used. Initially, the measurement number when $\Delta C \leq 0.5$ first occurred was determined, as indicated by the vertical blue dotted line. Next, at the determined measurement number, the difference in actual measured oxygen saturation ΔM between the two vessels can be determined. As shown in Figure 7, the value of ΔM is 4.6% for this dataset.

The value of ΔM may be different when the experiment is repeated under different conditions. For example, it may depend on vessel depth, hematocrit level, or other parameters that impact the contrast-to-background ratio of the data. Thus, the procedure to measure ΔM can be used to characterize additional factors that affect the ability to distinguish small differences oxygen saturation.
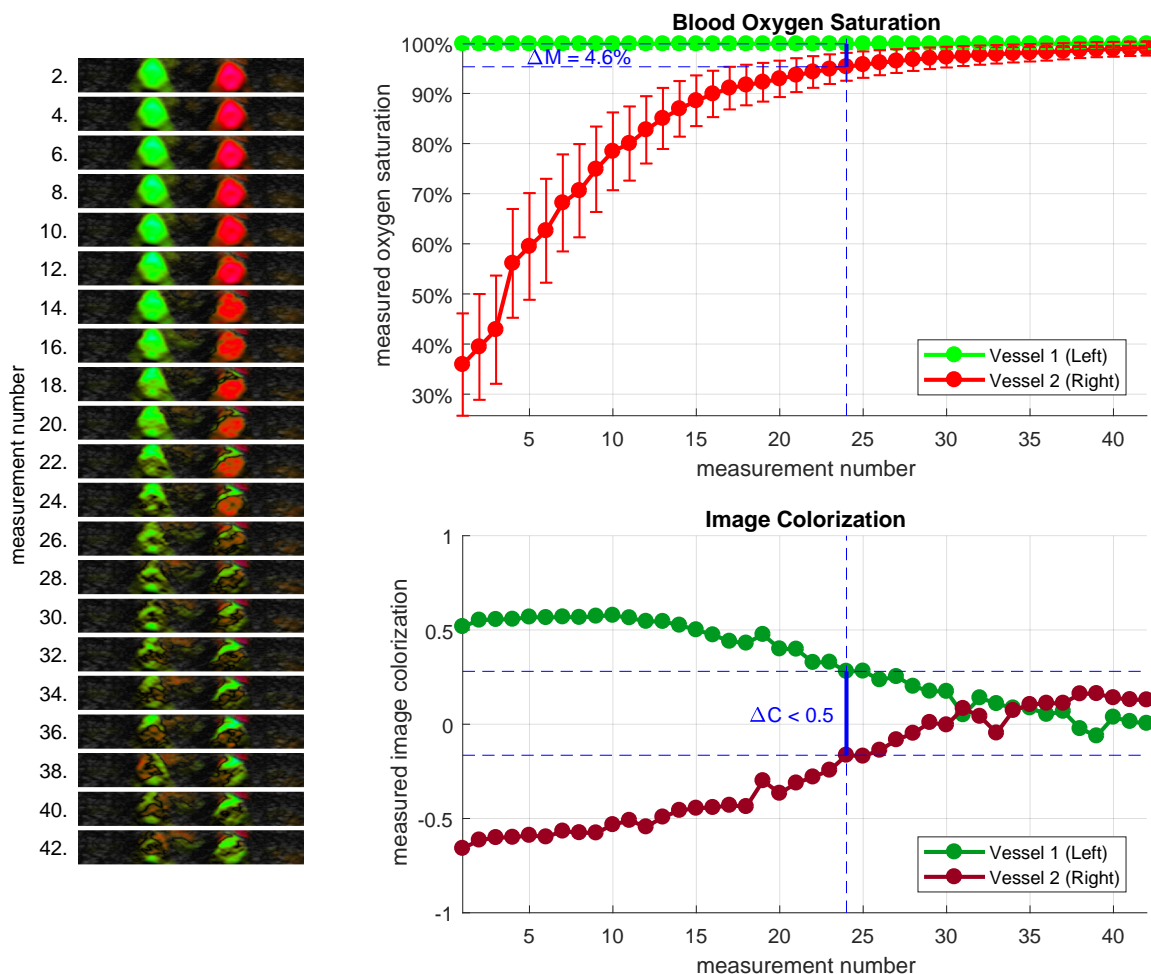

Figure 7: Ability to distinguish vessels in biologically relevant phantom. Colorization of Vessel 1 and Vessel 2 is displayed relative to average background reference level. Vessel 1 s_{O_2} level is held constant at full oxygenation. Vessel 2 s_{O_2} level is varied. Color mapping is determined statistically from s_{O_2} values in an image region containing both vessels and the phantom background material. High relative s_{O_2} appears green. Low relative s_{O_2} appears red. Mid-range s_{O_2} values become transparent. A *contrast distinction threshold* of $\Delta C = 0.5$ is reached for difference in *measured image colorization* at measurement number 24 (bottom). This occurs when the *measured oxygen saturation* difference ΔM is 4.6% (top).

5. CONCLUSION

We have presented a method for characterizing colorized opto-acoustic image maps that display spatial information regarding relative blood oxygen saturation level in tissue. A biologically relevant PVCP based phantom was constructed to mimic the optical properties of breast tissue. The phantom comprised two independently oxygenated vessels filled with bovine blood. A statistical mapping procedure was used to generate RGB colorization of opto-acoustic signal. A technique was proposed to quantify the ability to distinguish small differences in s_{O_2} when using maps with relative colorization. It was determined that measuring effects of additional parameters (vessel depth, hematocrit, etc.) on ΔM will be most effective if one reference vessel is held at constant s_{O_2} level while the other vessel is adjusted. In the PVCP phantom with reference vessel at 99% s_{O_2}, the image colorization threshold ΔC was reached at s_{O_2} difference ΔM of 4.6%. The spatial distribution of relative s_{O_2} is considered an important parameter for assessing differences between benign and malignant lesions. Characterization of measurement capabilities using materials similar to actual biological tissue may facilitate interpretation of color mapped images and how they relate to tumor physiology.

REFERENCES

[1] Yao, J. and Wang, L. V., "Photoacoustic tomography: fundamentals, advances and prospects," *Contrast media & molecular imaging* **6**(5), 332–345 (2011).

[2] Zackrisson, S., Van De Ven, S., and Gambhir, S., "Light in and sound out: emerging translational strategies for photoacoustic imaging," *Cancer research* **74**(4), 979–1004 (2014).

[3] Upputuri, P. K. and Pramanik, M., "Recent advances toward preclinical and clinical translation of photoacoustic tomography: a review," *Journal of Biomedical Optics* **22**(4), 041006 (2016).

[4] Valluru, K. S. and Willmann, J. K., "Clinical photoacoustic imaging of cancer," *Ultrasonography* **35**(4), 267 (2016).

[5] Valluru, K. S., Wilson, K. E., and Willmann, J. K., "Photoacoustic imaging in oncology: translational preclinical and early clinical experience," *Radiology* **280**(2), 332–349 (2016).

[6] Menezes, G. L., Pijnappel, R. M., Meeuwis, C., Bisschops, R., Veltman, J., Lavin, P. T., van de Vijver, M. J., and Mann, R. M., "Downgrading of breast masses suspicious for cancer by using optoacoustic breast imaging," *Radiology* , 170500 (2018).

[7] Neuschler, E., Butler, R., Young, C., Barke, L., Bertrand, M., Böhm-Vélez, M., Destounis, S., Donlan, P., Grobmyer, S., Katzen, J., et al., "A pivotal study of optoacoustic imaging to diagnose benign and malignant breast masses: A new evaluation tool for radiologists.," *Radiology* **287**(2), 398–412 (2018).

[8] Zalev, J., Clingman, B., Herzog, D., Miller, T., Ulissey, M., Stavros, A. T., Oraevsky, A., Lavin, P., Kist, K., Dornbluth, N. C., et al., "Opto-acoustic image fusion technology for diagnostic breast imaging in a feasibility study," in [*SPIE Medical Imaging*], 941909–941909, International Society for Optics and Photonics (2015).

[9] Oraevsky, A., Clingman, B., Zalev, J., Stavros, A., Yang, W., and Parikh, J., "Clinical optoacoustic imaging combined with ultrasound for coregistered functional and anatomical mapping of breast tumors," *Photoacoustics* **12**, 30–45 (2018).

[10] Zalev, J., Clingman, B., Smith, R. J., Herzog, D., Miller, T., Stavros, A. T., Ermilov, S., Conjusteau, A., Tsyboulski, D., Oraevsky, A. A., et al., "Clinical feasibility study of combined opto-acoustic and ultrasonic imaging modality providing coregistered functional and anatomical maps of breast tumors: Part II," in [*SPIE BiOS*], 858103–858103, International Society for Optics and Photonics (2013).

[11] Zalev, J., Clingman, B., Herzog, D., Miller, T., Stavros, A. T., Oraevsky, A., Kist, K., Dornbluth, N. C., and Otto, P., "Opto-acoustic breast imaging with co-registered ultrasound," in [*Medical Imaging 2014: Biomedical Applications in Molecular, Structural, and Functional Imaging*], **9038**, 90381J, International Society for Optics and Photonics (2014).

[12] Niederhauser, J. J., Jaeger, M., Lemor, R., Weber, P., and Frenz, M., "Combined ultrasound and optoacoustic system for real-time high-contrast vascular imaging in vivo," *IEEE transactions on medical imaging* **24**(4), 436–440 (2005).

[13] Emelianov, S. Y., Aglyamov, S. R., Shah, J., Sethuraman, S., Scott, W., Schmitt, R., Motamedi, M., Karpiouk, A., and Oraevsky, A. A., "Combined ultrasound, optoacoustic, and elasticity imaging," in [*Photons Plus Ultrasound: Imaging and Sensing*], **5320**, 101–113, International Society for Optics and Photonics (2004).

[14] Silverstein, M. J., Lagios, M. D., Recht, A., Allred, D. C., Harms, S. E., Holland, R., Holmes, D. R., Hughes, L. L., Jackman, R. J., Julian, T. B., et al., "Image-detected breast cancer: state of the art diagnosis and treatment," *Journal of the American College of Surgeons* **201**(4), 586–597 (2005).

[15] Vlahiotis, A., Griffin, B., Stavros, A. T., and Margolis, J., "Analysis of utilization patterns and associated costs of the breast imaging and diagnostic procedures after screening mammography," *ClinicoEconomics and outcomes research: CEOR* **10**, 157 (2018).

[16] Berg, W. A., Zhang, Z., Lehrer, D., Jong, R. A., Pisano, E. D., Barr, R. G., Böhm-Vélez, M., Mahoney, M. C., Evans, W. P., Larsen, L. H., et al., "Detection of breast cancer with addition of annual screening ultrasound or a single screening mri to mammography in women with elevated breast cancer risk," *JAMA* **307**(13), 1394–1404 (2012).

[17] Spirou, G. M., Oraevsky, A. A., Vitkin, I. A., and Whelan, W. M., "Optical and acoustic properties at 1064 nm of polyvinyl chloride-plastisol for use as a tissue phantom in biomedical optoacoustics," *Physics in Medicine & Biology* **50**(14), N141 (2005).

[18] Cook, J. R., Bouchard, R. R., and Emelianov, S. Y., "Tissue-mimicking phantoms for photoacoustic and ultrasonic imaging," *Biomedical optics express* **2**(11), 3193–3206 (2011).

[19] Vogt, W. C., Jia, C., Wear, K. A., Garra, B. S., and Pfefer, T. J., "Biologically relevant photoacoustic imaging phantoms with tunable optical and acoustic properties," *Journal of biomedical optics* **21**(10), 101405 (2016).

[20] Bohndiek, S. E., Bodapati, S., Van De Sompel, D., Kothapalli, S.-R., and Gambhir, S. S., "Development and application of stable phantoms for the evaluation of photoacoustic imaging instruments," *PloS one* **8**(9), e75533 (2013).

[21] Fonseca, M., Zeqiri, B., Beard, P., and Cox, B., "Characterisation of a phantom for multiwavelength quantitative photoacoustic imaging," *Physics in Medicine & Biology* **61**(13), 4950 (2016).

[22] Maneas, E., Xia, W., Ogunlade, O., Fonseca, M., Nikitichev, D. I., David, A. L., West, S. J., Ourselin, S., Hebden, J. C., Vercauteren, T., et al., "Gel wax-based tissue-mimicking phantoms for multispectral photoacoustic imaging," *Biomedical optics express* **9**(3), 1151–1163 (2018).

[23] Vogt, W. C., Zhou, X., Andriani, R., Wear, K. A., Garra, B. S., and Pfefer, J., "Performance evaluation of photoacoustic oximetry imaging systems using a dynamic blood flow phantom with tunable oxygen saturation," in [*Photons Plus Ultrasound: Imaging and Sensing 2018*], **10494**, 1049426, International Society for Optics and Photonics (2018).

[24] Vogt, W. C., Zhou, X., Andriani, R., Wear, K. A., Pfefer, T. J., and Garra, B. S., "Photoacoustic oximetry imaging performance evaluation using dynamic blood flow phantoms with tunable oxygen saturation," *Biomedical Optics Express* **10**(2), 449–464 (2019).

[25] Jain, R. K., "Determinants of tumor blood flow: a review," *Cancer research* **48**(10), 2641–2658 (1988).

[26] Zhang, H. F., Maslov, K., Sivaramakrishnan, M., Stoica, G., and Wang, L. V., "Imaging of hemoglobin oxygen saturation variations in single vessels in vivo using photoacoustic microscopy," *Applied physics letters* **90**(5), 053901 (2007).

[27] Xu, M. and Wang, L. V., "Photoacoustic imaging in biomedicine," *Review of scientific instruments* **77**(4), 041101 (2006).

[28] Oraevsky, A. A. and Karabutov, A. A., "Optoacoustic tomography," in [*Biomedical photonics handbook*], CRC Press (2003).

[29] Jacques, S. L., "Optical properties of biological tissues: a review," *Physics in Medicine & Biology* **58**(11), R37 (2013).

[30] Cheong, W.-F., Prahl, S. A., and Welch, A. J., "A review of the optical properties of biological tissues," *IEEE journal of quantum electronics* **26**(12), 2166–2185 (1990).

[31] Wang, L., Jacques, S. L., and Zheng, L., "Mcmlmonte carlo modeling of light transport in multi-layered tissues," *Computer methods and programs in biomedicine* **47**(2), 131–146 (1995).

[32] Prahl, S. A., van Gemert, M. J., and Welch, A. J., "Determining the optical properties of turbid media by using the adding–doubling method," *Applied optics* **32**(4), 559–568 (1993).

[33] Zijlstra, W. and Buursma, A., "Spectrophotometry of hemoglobin: absorption spectra of bovine oxy-hemoglobin, deoxyhemoglobin, carboxyhemoglobin, and methemoglobin," *Comparative Biochemistry and Physiology Part B: Biochemistry and Molecular Biology* **118**(4), 743–749 (1997).

[34] Clerbaux, T., Gustin, P., Detry, B., Cao, M., and Frans, A., "Comparative study of the oxyhaemoglobin dissociation curve of four mammals: man, dog, horse and cattle.," *Comparative biochemistry and physiology. Comparative physiology* **106**(4), 687–694 (1993).

[35] Dash, R. K. and Bassingthwaighte, J. B., "Blood HbO_2 and $HbCO_2$ dissociation curves at varied O_2, CO_2, pH, 2, 3-DPG and temperature levels," *Annals of biomedical engineering* **38**(4), 1683–1701 (2010). Corrected Version.

[36] Zalev, J. and Clingman, B., "Statistical mapping in an optoacoustic imaging system," (May 3 2016). US Patent 9,330,452, Filed: March 11, 2013, Issued: May 3, 2016.